

Electron Gun-Based Active Charge Control of Nearby Spacecraft

James D. Walker III^{1b} and Hanspeter Schaub^{1b}

Abstract—The development of touchless active charge control (ACC) techniques for a neighboring spacecraft is an important step for testing and implementing space-based electrostatic actuation methods, such as debris removal with the electrostatic tractor (ET). A feedback controller is developed to manipulate the floating potential of a conducting target in a vacuum chamber by modulating the energy of the electron gun. A numerical charging model is developed, integrating the controller into a simulated environment consisting of the electron beam, secondary electron emission, and backscatter electron emission. This control is analytically proved to be stable for small deviations from the equilibrium charging state. Experiments conducted in a vacuum chamber environment are used to validate the numerical charge control model and demonstrate target ACC in an idealized laboratory scenario. Using the validated model, a numerical analysis is performed to confirm the derived stability condition and explore the charging behavior. Finally, uniformly sampled Monte Carlo trials are used to demonstrate that this control is robust to uncertainty in the electron beam impact current and the target material properties, an important aspect for in situ applications.

Index Terms—Charge control, electron beam, spacecraft charging, target charging.

I. INTRODUCTION

WHEN exposed to the space environment, the local electrons, ions, and photons cause electrostatic potentials to be generated on the surface of a spacecraft. Depending on the region of space the satellite's orbit traverses, this potential can range from tens of volts positive to tens of kilovolts negative: a high-density, low-energy plasma like in low-Earth-orbit (LEO) typically results in very low level charging (a few volts in magnitude) while potentials in auroral latitudes can reach hundreds of kilovolts even at low altitudes [1]. Spacecraft charging is important at or near geosynchronous orbits (GEOs) due to high-energy particles and low plasma density: the high-energy particles cause large electrostatic potentials and the low plasma density results in Debye lengths, the distance at which

Received 18 August 2025; accepted 23 October 2025. Date of publication 11 November 2025; date of current version 15 December 2025. This work was supported in part by the Department of Defense (DoD) through the National Defense Science and Engineering Graduate (NDSEG) Fellowship Program and in part by the Air Force Office of Scientific Research (AFOSR) under Grant FA9550-23-1-0570. The review of this article was arranged by Senior Editor C. A. Ekdahl. (Corresponding author: James D. Walker III.)

The authors are with the Department of Aerospace Engineering Sciences, Colorado Center for Astrodynamics Research, University of Colorado Boulder, Boulder, CO 80303 USA (e-mail: James.WalkerIii@colorado.edu).

Color versions of one or more figures in this article are available at <https://doi.org/10.1109/TPS.2025.3627474>.

Digital Object Identifier 10.1109/TPS.2025.3627474

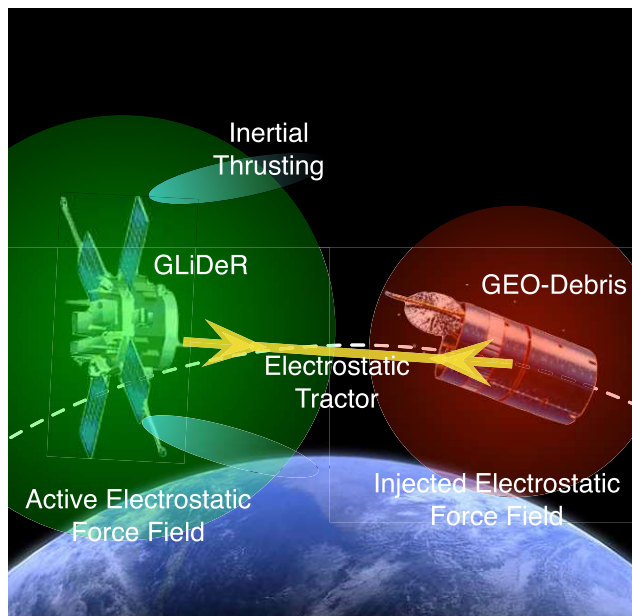


Fig. 1. Illustration of the GEO GLiDeR concept using the electrostatic tractor (ET) [15].

a charged object can electrically affect another, up to hundreds of meters [1], [2], [3]. Additionally, the near-GEO region is home to many high-value GPS and communication satellites. With the growing global goal of expanding human presence and influence around the moon [4], [5], [6], [7], the importance of spacecraft charging in cislunar regions is becoming more prominent in addition to the geosynchronous region. Satellites in lunar orbits will experience variable charging behavior, including Debye lengths ranging from 10 m to greater than 100 m [8], [9]. The work in this article is most applicable to GEO and cislunar regions, where low fluxes of high-energy plasma lead to kilovolt charging levels with large Debye lengths. The LEO regime experiences cold and dense plasmas that make active charging very power-prohibitive.

For an isolated spacecraft orbiting in these regions, there are two major concerns regarding spacecraft charging: electrostatic discharges (ESDs) and interference with instrument measurements [1], [10]. ESD events occur when a significant amount of charge rapidly transfers between neighboring surfaces, causing damage that can range from disturbing telemetry signals to physical damage to onboard electronics [1]. An analysis of pulses measured on the SCATHA mis-

sion first determined that ESD events occur in regions with high-energy plasma, leading to multiple mitigation techniques for ESDs being implemented in situ, including solar panel cover glass and designing fully conductive spacecraft [11], [12], [13]. Spacecraft charging also interferes with measurements of plasma density, mean energy, and distribution. Charged particles are accelerated/decelerated as they penetrate through the spacecraft's electric field and are measured by the onboard instruments. A low-energy "hidden ion population" was discovered from data collected by the ATS 6 and SCATHA missions [14]. It was revealed that, near the inner edge of the plasma sheet, there exists a population of 1 eV ions that could only be measured in eclipse, when the potential of the spacecraft drops below 5 V [14]. Otherwise, they are not energetic enough to penetrate the electric field of the spacecraft and be measured. For nearby spacecraft, additional effects of spacecraft charging occur. As two charged objects approach each other, significant electrostatic forces and torques are generated between them [16], [17], causing inefficiencies in relative motion controllers [18], [19], [20]. During docking missions, there is also a risk of ESD events between the two crafts [20]. While these additional perturbations introduce concerns to proximity and docking operations, they also offer the unique ability of contactless maneuvers. Coulomb formation flying takes the Coulomb forces between charged spacecraft and uses them to reconfigure spacecraft formations without propellant [21]. More recently, electrostatic detumbling has been explored. It has been shown that, for a two-spacecraft system, the potential and attitude of a servicing spacecraft can be manipulated and used to apply controlled electrostatic torques to an uncontrolled target, reducing its angular momentum [22], [23], [24]. Finally, the ET is a novel method proposed for large debris removal from GEO orbits [15], [25]. The ET uses a servicing spacecraft equipped with an electron beam to apply a strong negative current to a target while generating a positive current on itself [15], [25]. By applying opposite charges to a servicing spacecraft and an uncontrolled debris object, an attractive Coulomb force is generated between them, allowing the servicer to manipulate the motion of the debris object [15]. A concept figure of this is shown in Fig. 1. Using this "ET," the servicer is then able to tug the debris to a graveyard orbit where it will no longer pose a risk to other GEO satellites [15]. In previous work, it was found that implementing the ET would allow for a multi-ton debris object to be re-orbited in a matter of months [26]. However, this prior ET performance work assumed that the spacecraft potentials were controlled to desired values, and the physical process of active charging was not considered.

A key aspect of electrostatic actuation is the ability to control the electrostatic force generated between the two objects [15]. This requires the potential of both the servicer and the target to be actively maintained. In this article, active charge control (ACC) refers to the use of one or more controlled currents to apply a desired potential to an object. The ATS and SCATHA missions were some of the first missions to explore ACC of the spacecraft's own potential in situ: ATS 5 used a hot filament electron emitter to expel a negative current, while ATS 6 used a neutral plasma emitter [27], [28], [29]. Both were

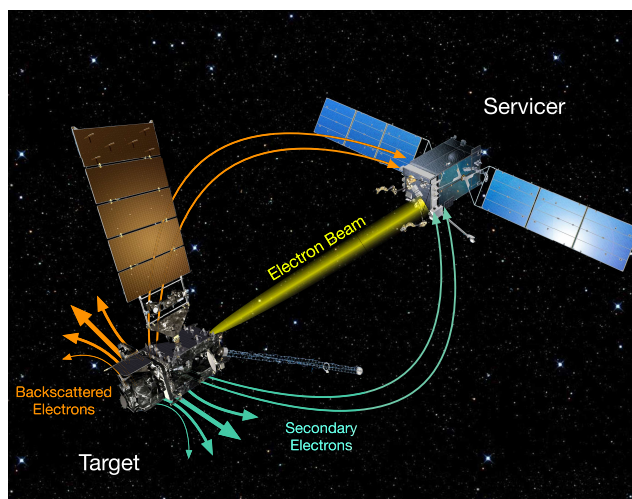


Fig. 2. Illustration of ACC of a target spacecraft.

successful in driving the spacecraft's potentials closer to 0 V, but the neutral plasma emitter yielded more consistent results [27], [29]. SCATHA demonstrated ACC on itself using both an electron emitter and an ion emitter [28]. After the discovery of low-energy plasma populations, more missions were equipped with ACC devices, so the entire range of energetic plasma could be measured, including GeoTail, Cluster, Double Star, and MMS [30], [31], [32], [33], [34], [35].

The majority of ACC research so far has focused on manipulating the electric potential of a single controlled spacecraft; however, electrostatic actuation techniques, such as the ET, require ACC of a target as well. Previous touchless spacecraft ACC research exploring multisatellite electrostatic maneuvers has either focused on numerical analysis or used high-voltage power supplies to force objects to the desired values for experimental investigations [15], [36], [37]. This article researches a method for contactless driving an uncontrolled floating target in a vacuum chamber to a desired potential using an externally mounted electron gun. This is a significant step forward for spacecraft ACC research, as the vacuum chamber object's potential is now allowed to change according to the electron beam parameters. The experimental results are compared to numerical models of this test setup to make analytical predictions of the observed charging behavior. Using the same setup as proposed for the ET, the servicing spacecraft is equipped with a high-energy electron beam [15]. With the ET concept, the target is irradiated with high-energy electrons. The dominating negative current onto the target charges it significantly negative, while the servicer emission of the negative particles charges it positive [1], [15]. In this article, only one object is in the vacuum chamber to focus on the target charging behavior. The high-energy electron gun is mounted externally to the grounded chamber and does not cause an object to charge positively in this setup. The vacuum chamber is also equipped with a vacuum ultraviolet (VUV) lamp to experimentally simulate the photoelectron current. By taking a measurement of the target's potential using a high-voltage probe inside the chamber and knowing the desired potential, a feedback controller is developed and applied to the electron beam. The e-beam parameters are adjusted, altering

the net current applied to the target and, therefore, its potential. Fig. 2 presents a concept image of the envisioned space-based target ACC using an electron beam. The scope of this article is limited to using the high-voltage probe to get accurate potential measurements. No space plasma interactions are modeled at this time. This allows the study to focus on the e-beam-controlled charging behavior. Prior research has developed methods based on measuring the secondary electron emission [38] or X-ray Brehmstrahlung [39] resulting from the e-beam hitting the target's metallic surface. Future work will investigate incorporating such touchless potential sensing methods into the ACC experiments. The scope of this study is to focus on developing a controller to touchlessly control the potential of a vacuum chamber's metallic object and investigate its robustness and effectiveness.

This article presents two methods for contactless target ACC, implements and compares both methods, develops a simulation framework, and validates this framework with experiments conducted in a vacuum chamber environment. Section II outlines the spacecraft charging framework and feedback controller used throughout this article. Section III describes the experimental setup used to validate the developed model, and in Section IV, experiments for both methods are presented. The results of the simulations are compared to the experimental results, and the stability condition of the control is derived in Section V. The effect of uncertainty on the control scenario is investigated using Monte Carlo sampling in Section V as well.

II. NUMERICAL METHODS

A. Overview of the Spacecraft Charging Model

The following overview of spacecraft charging is based on information presented in [1].

When exposed to the space environment, a fully conducting spacecraft acts as a capacitor and its charging behavior is governed by Ohm's law

$$\frac{d\phi(t)}{dt} = \frac{I_{\text{net}}(t)}{C_{\text{sc}}} \quad (1)$$

where the rate of change of the potential, ϕ , of an object is dependent on the net current reaching the spacecraft surface, I_{net} , and the capacitance, C_{sc} , of the object. While the object is exposed to the space environment, it experiences a variety of currents that cause its potential to change. This charging continues until it reaches an equilibrium point where all the currents balance to $I_{\text{net}} = 0$; at this point, the object has reached its natural *floating potential*.

An electron gun emits a stream of high-energy electrons that impact the target's surface. This results in the target experiencing a negative current, decreasing its electrostatic potential. However, if the electron energy is smaller than the difference between the electric potentials of the servicer and target spacecraft, then the emitted electrons do not have enough energy to reach the target and are attracted back to the servicing spacecraft. The current impacting the target can be expressed as the following pairwise function:

$$I_T(\phi_T, E_{\text{EB}}, I_{\text{EB}}) = \begin{cases} -I_{\text{EB}}, & \phi_S - \phi_T < E_{\text{EB}} \\ 0, & \phi_S - \phi_T \geq E_{\text{EB}} \end{cases} \quad (2)$$

where E_{EB} is the energy of the emitted electrons and ϕ_S and ϕ_T are the potentials of the servicer and the target, respectively. Additionally, I_{EB} is the current leaving the electron beam. For the experiments presented here, the electron emitter is attached to the grounded vacuum chamber enclosure, meaning $\phi_S = 0$ V. If only (2) is considered, this suggests that the target should charge to $\phi_T = -E_{\text{EB}}$; however, this is not the case due to electron beam-induced secondary electron and backscattered electron emissions.

When an electron impacts the surface of a target, it can transfer its energy to the surface electrons. If the impacting (primary) electron transfers enough energy, the surface electron is emitted from the target as a secondary electron. The probability of a secondary being emitted, the secondary electron yield (SEY), is a function of electron impact energy, E , and is denoted as $\delta(E)$. Depending on the material of the target, $\delta(E)$ can exceed one, indicating that more than 1 secondary electron is emitted for a single primary electron. When this occurs, the net current is positive and the target charges accordingly. In the case of these vacuum chamber experiments, a mono-energetic electron beam is being used, so it can be assumed that the electron gun emits electrons at a single predetermined energy. When the primary electron is emitted from an electron beam, the impact energy is determined by

$$E = E_{\text{EB}} + \phi_T. \quad (3)$$

For a given surface area, the secondary electron current, I_{se} , generated by an electron beam with energy E_{EB} and current I_{EB} is

$$I_{\text{se}}(E, I_{\text{EB}}) = \delta(E) I_T(E, I_{\text{EB}}). \quad (4)$$

Multiple methods have been developed for determining $\delta(E)$ of a given material [40]. The method developed by Sanders and Inouye is used in this article because the SEY properties of gold are readily available [1]. Other common methods for SEY estimation are those developed by Draine [41] and the four-parameter fit used by NASCAP and SPIS [42], [43]. The SEY given by the Sanders and Inouye model is

$$\delta(E) = c \left[\exp\left(\frac{-E}{a}\right) - \exp\left(\frac{-E}{b}\right) \right] \quad (5)$$

where a , b , and c are defined as $a = 4.3E_{\text{max}}$, $b = 0.367E_{\text{max}}$, and $c = 1.37\delta_{\text{max}}$ [44]. Here, δ_{max} is the maximum yield and E_{max} is the energy at which the maximum yield occurs.

Backscattered electrons are also generated by e-gun electrons. Unlike secondary electrons, backscattered electrons do not transfer their energy. Instead, as the primary electron approaches the target, it is reflected, or backscattered away. This typically occurs around ion sites in the material, where the high concentration of electrons repels the primary electron. Because the backscattered electron is the same as the primary electron, the ratio of incoming to outgoing electrons can never exceed 1. Similar to secondary electrons, the backscattered electron current is determined by a material property, backscattered electron yield (BEY), denoted $\eta(E)$. The BEY used in this article is proposed by Prokopenko and Laframboise

$$\eta(E) = A - B \exp(-CE) \quad (6)$$

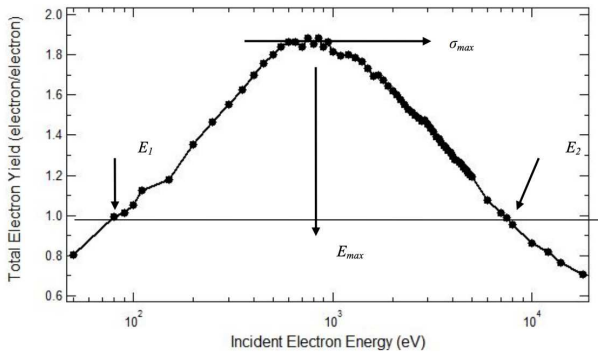


Fig. 3. TEY of polycrystalline gold as determined by [46].

where A , B , and C are constants determined by the material [45]. Similarly, the backscattered electron current generated by an electron beam is

$$I_{be}(E, I_{EB}) = \eta(E) I_T(E, I_{EB}). \quad (7)$$

It is important to note that both SEY and BEY depend on the incident angle of the impacting electrons. The equations given here are for a normal incidence angle, the same angle used in the experiments.

Because SEY and BEY are both functions of energy, they are often summed together and given the name total electron yield (TEY). Fig. 3 presents the TEY for polycrystalline gold as a ratio of outgoing to incoming electrons vs impact energy of the electron based on experimental data [46].

The last significant current the target experiences in these experiments is photoelectric. When energetic photons impact the surface of a target, they can be absorbed by the surface electrons, moving the electrons to an excited state. If the energy of the photon is greater than the work function of the target material, the electron is emitted, similar to secondary electrons. This emission of photoelectrons generates a positive current. Because photoelectrons are emitted with low energies, they act similarly to secondary electrons: charging the target slightly positively and then being attracted back. The photoelectron current flux is given in [1] as

$$J_{ph} = \int_0^{\infty} Y(\omega) f(\omega) d\omega. \quad (8)$$

Here, $Y(\omega)$ is the photoelectric yield of the material and $f(\omega)$ is the photon energy distribution. Equation (8) is integrated over the photon energy, ω , and the total photoelectron current, I_{ph} , can be found for a known surface area.

These currents are summed together to obtain the net current experienced by the target

$$\begin{aligned} I_{net}(\phi_T, E_{EB}, I_{EB}) = & -I_T(E, I_{EB}) \\ & + \delta(E) I_T(E, I_{EB}) \\ & + \eta(E) I_T(E, I_{EB}) + I_{ph}(\phi_T). \end{aligned} \quad (9)$$

It can be seen that the net current depends on two beam parameters: the beam current and beam energy. This leads to the two methods of target ACC presented here: current ACC (CACC) and energy ACC (EACC). The goal of both of these methods is to manipulate the control parameter such that, once

ϕ_T reaches the desired potential, the net current applied to the target becomes 0 A.

Hammerl and Schaub [47] discovered that charging a target with only an electron gun can, under the right conditions, generate up to three equilibrium points, two of which are stable: if a target starts at 0 V and is irradiated with an electron gun, the final potential may be different than if the initial potential is a significantly negative value [47]. However, this applies to spacecraft in a single Maxwellian plasma. For this article, charge control is only considered in a vacuum chamber environment, so the conditions for the second stable equilibrium point are not met.

B. Contactless Target ACC

The goal of contactless target ACC is to adjust the parameters of the electron beam such that, when the potential of the target is at the desired goal potential, the net current acting on the target is 0 A. Plugging (9) into (1) gives the differential equation that defines the charging behavior of the target

$$\begin{aligned} \frac{d\phi_T(t)}{dt} & = \frac{I_T(I_{EB})}{C_{sc}} (-\delta(\phi_T, E_{EB}) - \eta(\phi_T, E_{EB}) + 1) + \frac{I_{ph}(\phi_T)}{C_{sc}}. \end{aligned} \quad (10)$$

Examining (10), two segments are influenced by the electron beam parameters: $I_T(I_{EB})$ and $(-\delta(\phi_T, E_{EB}) - \eta(\phi_T, E_{EB}) + 1)$. The third component, I_{ph} , is not controlled by the e-beam. The methods of the target ACC will focus on these two e-beam-influenced components. It is important to note that, because the main instrument of this control is an electron beam, only negative potentials and potentials of a few volts positive can be achieved.

1) *E-Beam Current-Based ACC*: The first target ACC technique is CACC and involves the first term: controlling I_{EB} while E_{EB} is held constant. Because $d\phi_T(t)/dt$ depends directly on I_{EB} , if the target potential is too positive, the current is increased, driving the target more negative. However, the opposite is not true: the current cannot be adjusted to charge a target positive. To account for this in the vacuum chamber experiments, a VUV lamp applies a continuous I_{ph} . When the control overshoots and charges the target too negatively, the beam current is decreased, and the photoelectron current charges the target positively.

Control is only applied to the current of the electron beam; more specifically, the change in the beam current. For this derivation, it is assumed that $-\phi_T < E_{EB}$, such that $I_T = -I_{EB}$. If this is not the case, then $I_{EB} = 0$. Defining the state vector as the target potential and beam current gives the differential equation

$$\dot{\mathbf{x}} = \begin{bmatrix} \dot{\phi}_T \\ \dot{I}_{EB} \end{bmatrix} = \begin{bmatrix} \frac{I_{EB}}{C_{sc}} (\delta(E) + \eta(E) - 1) + \frac{I_{ph}}{C_{sc}} \\ 0 \end{bmatrix} + \begin{bmatrix} 0 \\ u \end{bmatrix} \quad (11)$$

with

$$\begin{aligned} \delta(E) & = c \left[\exp\left(\frac{-(E_{EB} + \phi_T)}{a}\right) - \exp\left(\frac{-(E_{EB} + \phi_T)}{b}\right) \right] \\ \eta(E) & = A - B \exp(-C(E_{EB} + \phi_T)). \end{aligned}$$

This is the nonlinear equation that governs charging behavior when a target is exposed to CACC. There is no control applied directly to the target potential; its charging is a natural response to the e-beam current control. The beam current, on the other hand, has no natural dynamics and is completely determined by the controller.

For CACC, a proportional and derivative control is explored. The control depends on the difference between the goal and actual potential (the error) and rate of change of the target potential

$$u = K_P (\phi_T - \phi_G) + K_D \frac{\phi_{T_{i+1}} - \phi_{T_i}}{\Delta t} \quad (12)$$

where ϕ_T is the measurement of the target's potential, ϕ_G is the goal potential, and K_P (a positive value) and K_D (a negative value) are the proportional gain and derivative gain, respectively. The measurement time is Δt . When the target potential is too negative, the error is negative and the current decreases. The opposite is true for a positive error. Also, if the target potential decreases quickly, the derivative control reduces the applied control. This allows the control to converge faster by having a larger proportional gain without the system being underdamped. A measure of the target's electric potential is taken using a high-quality electrostatic probe such that the voltage measurement errors are small and can be ignored in this study.

2) *E-Beam Energy-Based ACC*: The second method of ACC, EACC, varies the energy of the electron beam while I_{EB} is held at a constant value and involves the second term from (10): $(\delta(\phi_T, E_{EB}) + \eta(\phi_T, E_{EB}) - 1)$. Adjusting the beam energy can charge a target either positive or negative, so VUV lamps are unnecessary and $I_{ph} = 0$. This control takes advantage of the natural equilibrium of the TEY.

Fig. 3 shows that, for gold, there are two impact energies where the ratio of electrons is 1. At these two energies, assuming only e-beam-related currents, the number of incoming and outgoing electrons is equal: no net current is acting on the target, and its potential is at equilibrium. Of these two ‘‘crossover energies,’’ only one of them is stable. The first crossover energy, E_1 , is unstable. If $E < E_1$, the target experiences a negative current, and the impact energy is driven away from E_1 . On the other hand, if $E > E_1$, the target experiences a positive current, again driving the impact energy away from E_1 . The opposite is true for E_2 . When $E > E_2$, TEY is less than 1, $d\phi_T/dt$ is negative, and the impact energy is driven toward E_2 . When $E < E_2$, TEY is greater than 1, $d\phi_T/dt$ is positive, and the impact energy is again driven toward E_2 . By only controlling the beam energy, the electron beam can apply either a positive or negative current to drive the system to this stable equilibrium. A more in-depth explanation of this phenomenon is given in [1, Ch. 9].

An important note here is that if $E_1 < E_{EB} \leq E_2$, the target will charge to near-zero. In this region, the sum of the secondary and backscattered electron currents is greater than the impacting beam current, so there is a net positive number of electrons emitted from the target. However, secondary electrons are emitted with low energy (< 10 eV). As the target charges slightly positively, the secondary electrons are attracted back to the target. Therefore, the target cannot charge

more than a few volts positive. Backscattered electrons are emitted with energy equal to the impact energy, but $\eta(E) \leq 1$ and cannot charge the target positively on its own.

Because E_2 is determined by material properties (SEY and BEY properties), it is constant for a given setup. Returning to (3), at this equilibrium, $E = E_2$ and, therefore, the difference between the electron energy and target potential also has to be constant at equilibrium ($E_{EB} + \phi_T = E_2$). This gives a direct relationship between electron beam energy and target potential: increasing the beam energy will increase the target potential by the same amount, $\Delta\phi_T = \Delta E_{EB}$, at a steady state.

For EACC, control is applied to the change in beam energy. Defining the state vector as the target potential and beam energy gives a very similar equation as (11)

$$\dot{\mathbf{x}} = \begin{bmatrix} \dot{\phi}_T \\ \dot{E}_{EB} \end{bmatrix} = \begin{bmatrix} \frac{I_{EB}}{C_{sc}} (\delta(E) + \eta(E) - 1) \\ 0 \end{bmatrix} + \begin{bmatrix} 0 \\ u \end{bmatrix} \quad (13)$$

again with

$$\delta(E) = c \left[\exp\left(\frac{-(E_{EB} + \phi_T)}{a}\right) - \exp\left(\frac{-(E_{EB} + \phi_T)}{b}\right) \right]$$

$$\eta(E) = A - B \exp(-C(E_{EB} + \phi_T)).$$

The only differences between the two equations for charge control are the state vector and the photoelectron current.

For EACC, the same linear PD controller shown in (12) is implemented. Again, to apply this control, u is added to the electron beam parameter. When the target is more positive than the goal potential, $\phi_T - \phi_G < 0$, the resulting error is positive, increasing the beam current/energy and thereby decreasing the target potential. When the opposite occurs and $\phi_T - \phi_G > 0$, the error is negative, resulting in a lower beam current/energy.

A simulation framework applying this control to the charging equations is developed and used to explore ACC numerically. To have confidence in the numerical model, vacuum chamber experiments are conducted and compared to the simulations.

III. EXPERIMENTAL SETUP

Experiments for this project were conducted in the JUMBO vacuum chamber at the Air Force Research Labs [48]. The experimental setup includes a Faraday cup, an electrostatic voltmeter, and a 4-in diameter gold-plated copper disk. Fig. 4 shows the experimental setup used throughout this article.

The target object in these experiments is a gold-plated copper disk. Secondary and backscattered electron generation is a significant factor in charging experiments: they generate a current on the target surface that is difficult to account for because the TEY is dependent on material properties and surface topology [1], [40], [49]. A copper disk is chosen as the target object; however, copper oxidizes quickly in air, altering the material properties. To account for this, the copper disk is sputter-coated with a 100-nm gold layer, which is not reactive with air. This ensures the surface properties do not change as the sample is exposed to air, making experiments more repeatable than using a pure copper sample. Due to the size constraints of the sputter-coating machine, a uniform thickness of the gold coating is not guaranteed. Fig. 3 shows the TEY for

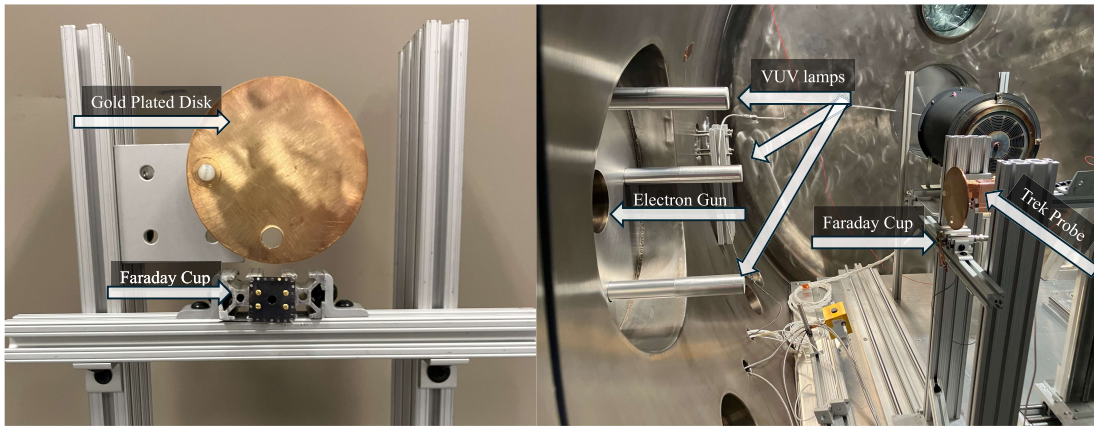


Fig. 4. Experimental setup used throughout this project. Portion exposed to the electron beam and VUV photons (left). Image inside the vacuum chamber (right).

polycrystalline gold experimentally determined in [46]. The crossover points, E_1 and E_2 , occur at ≈ 80 V and ≈ 7 kV for gold, respectively. In this article, the minimum electron beam energy used is 2 keV and $E \gg E_1$; therefore, the impact energy of the electrons is always driven to E_2 . Ceramic standoffs and nylon screws were used to electrically isolate the disk from the rest of the setup, creating a floating target.

The values for the SEY and BEY of gold used in this project are given in [1, Ch. 3] as $\delta_{\max} = 1.45$, $E_{\max} = 0.8$ kV, $A = 0.4801$, $B = 0.3566$, and $C = 0.6103$. The exact value for these material properties depends on surface roughness, contamination layers, and so on and will likely not be exact compared to the target used in experiments; however, they are a good approximation of these values.

The high-energy electron gun used in these experiments was a Kimball Physics EGPS-8105UD and is capable of generating electrons with energies up to 100 keV. For these experiments, the maximum beam energy used is 12 keV. In front of the cathode of the electron gun is a grid that, when a potential of 500 V is applied to it, keeps all electrons from being emitted; they are not energetic enough to penetrate the electric field of the grid. If less than 500 V is applied, some electrons may escape the electron gun. This depends on the energy of the emitted electrons. By adjusting the voltage on this grid, the flux of electrons emitted from the beam can be controlled: the higher the grid voltage, the fewer electrons emitted. This is used to implement the current control method rather than control the current directly, as this is safer for the electron gun.

Three identical KrLM-L VUV sources from Resonance LTD are used to excite photoelectrons from the target during the current control experiments. The gold surface of the target object has a work function of 5.5 eV and the underlying copper has a work function of 4.1 eV [50]. With energies of 10.1 and 10.6 eV, the VUV photons are more energetic than the work functions and can excite electrons from the target surface. These lamps are not connected to the computer and can only be manually turned off and on; therefore, no control is applied to the VUV lights. The photoelectric current given off by the VUV lamps is estimated using a UV light detector. With all three lamps on, a positive current of ≈ 2.5 nA is applied to the target.

A Faraday cup is positioned near the gold-plated disk to measure the flux of electrons from the electron beam. This measurement is sufficient for an initial approximation of I_T , the current impacting the target. Care was taken to ensure that the plate was not obstructing the aperture of the Faraday cup. The Faraday cup is aligned with the center of the electron gun aperture.

A Trek electrostatic voltmeter provides a contactless measurement of the target's potential. This probe functions as follows: the probe is placed roughly 3 mm from the target and, as the potential across the plate changes, a power supply drives the electric field between the target and the probe to zero, thereby achieving the same voltage on the probe as is on the plate. With a range of ± 20 kV and a resolution of 20 V, the Trek probe can accurately measure any potentials that are applied during these experiments at a rate of 1.2 s. All metal (except for the disk) is grounded to reduce interference between the probe and the plate. The equipment is controlled, and data is stored remotely through a LabVIEW interface.

IV. EXPERIMENTAL RESULTS

Vacuum chamber experiments are used to demonstrate the potential of CACC and EACC in an idealized scenario.

A. Floating Potentials

To get an estimate of the second crossover energy of the system, the steady-state floating potentials achieved by multiple beam energies are determined. This characterization is used to inform the numerical simulations and provides a first look at how the electron beam energy control functions. Fig. 5 presents the relationship between the electron beam energy and floating potential for the given experimental setup.

There are two distinct regions in Fig. 5(a). For beam energies greater than 7 keV, the relationship between target potential and beam energy is linear with a slope of -0.87 . Using these data points, the E_2 value of the system is estimated to be 6.32 keV. This is consistent with the TEY from [46] with an error of 9.8%. For beam energies less than 7 keV, the behavior is nonlinear, which is also expected. As described in Section II, charging should not occur until the beam energy

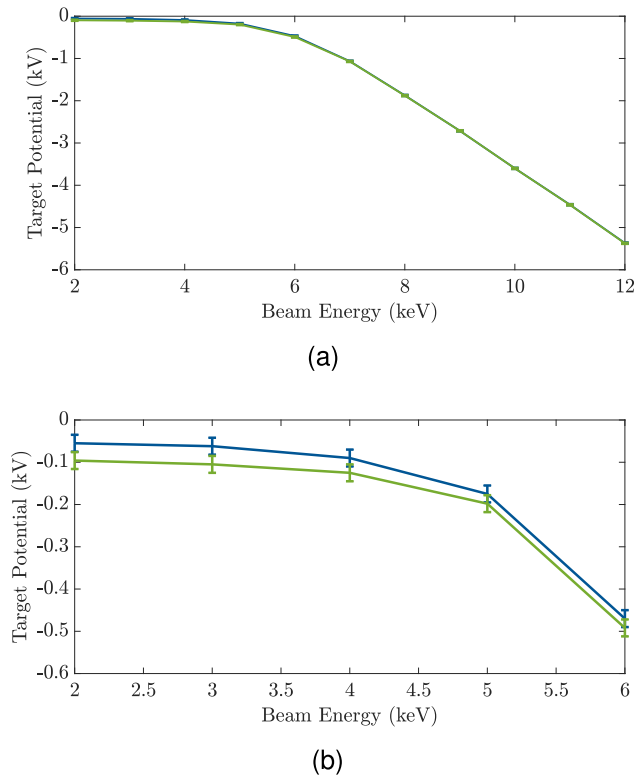


Fig. 5. Floating potentials generated on the target for beam energies ranging from 2 to 12 keV for two separate trials. (a) All beam energies. (b) Lower beam energies.

exceeds E_2 , at which point it then should increase linearly. However, there is a charge at beam energies lower than 6.32 keV. This is caused by secondary electrons generated in the copper oxide layer. Using the formula presented in [51] for gold, the maximum penetration depth of a 5-keV electron is 222 nm [52]. The gold layer is only 100-nm thick, which means some secondaries may be generated from the copper/copper oxide layer of material. The SEY of copper oxide is not well characterized, but based on the measurements of pure copper and copper after air exposure [49], [53], it is reasonable to conclude that E_2 for copper oxide is less than that of gold and greater than 3 keV. According to Fig. 5(b), significant charging occurs between 4 and 5 keV. The average penetration depth of 6 keV electrons into gold is around 25 nm, so most electrons never make it into the copper, but because secondaries are only generated from the copper layer at this energy, they dominate the charging behavior [54], [55]. Once the beam energy exceeds 6 keV, secondaries are excited from the gold layer as well. Significantly more electrons are emitted from the gold layer and therefore dominate the charging behavior. Additionally, when the beam energy is less than 4 keV, it is expected that the target has a slightly positive (a few volts) potential; this discrepancy is likely due to inconsistencies with the Trek Probe. When measuring near 0-V potentials, the Trek Probe measurement would drift slightly negative. Once a significant potential was achieved on the target, this drifting would stop.

From the floating potential results, the most significant conclusion is that the linear charging behavior described by the

TABLE I
CONVERGENCE BEHAVIOR OF CACC WITH VARYING EXPERIMENTAL PARAMETERS

E_{EB} (keV)	ϕ_G (kV)	K_P (10^{-4})	K_D	Convergence Time (s)	Steady State Max Error (V/%)
9	-2	-5	1	41.9	28/1.4%
9	-2	-10	1	37.1	44/2.2%
9	-2	-5	2	26.3	24/1.2%
9	-2	-10	2	19.1	26/1.8%
10	-1	-5	1.8	21.5	47/4.7%
10	-2	-4	0	126.9	90/4.5%
10	-2	-5	0	136.4	108/5.4%
10	-2	-6	0	202.2	104/5.2%
10	-2	-4	1.8	20.3	30/1.5%
10	-2	-5	1.8	14.4	40/2.0%
10	-2	-10	1.8	62.2	38/1.9%
10	-2	-20	1.8	51.4	1,216/60.8%
10	-3	-5	1.8	31.1	24/0.8%

TEY equations only occurs once the landing energy exceeds 6.32 keV, or when the target potential exceeds ≈ 500 V. This is important for comparing experimental results to numerical results because the assumptions made in the numerical simulations will only hold when the target is in the linear region of charging.

B. Current-Based ACC

For CACC, trials were conducted using both the proportional control and the derivative control. The charging behaviors of multiple CACC scenarios are presented in Table I, including different beam energies, goal potentials, and gains. In each of these trials, the starting target potential was ≈ 0 V. It can be noticed that in Table I, K_P is a negative value and K_D is positive, as opposed to previously stated. Because the control is applied to the grid of the electron gun, and increasing the grid potential decreases the beam current, the signs of the gains had to be flipped in these experiments. The exact charging behavior depends significantly on the selected gains. For this data, the gains are tailored for a 10-keV beam with a goal potential of -2 kV. From there, the scenario parameters are varied to demonstrate how each one affected the convergence times and steady-state errors. Across each charging scenario, steady-state behavior is achieved and, for most trials, the error at the steady state is less than 6%. The only trial where this is not true is a 10-keV beam energy with a $K_P = -20 \times 10^{-4}$: the proportional gain is large and creates large oscillations at the steady state. Also, without derivative gain, the convergence times increase nearly tenfold. This is expected because the resulting control is underdamped. Interestingly, the error at the steady state is only around 5% without derivative control.

Fig. 6 presents experimental data of two separate trials for three scenarios. Every scenario has the setup outlined in Section III, with gain values of $K_P = -5 \times 10^{-4}$ and $K_D = 1.8$. Each scenario converges in 15–30 s and the control appears to be consistent across each trial. Trials with $\phi_G = -2$ kV are close to critically damped with a convergence time of 20 s. In contrast, trials with $\phi_G = -1$ kV are slightly underdamped, converging after 24 s, and trials with $\phi_G = -3$ kV are slightly overdamped with a convergence time of 32 s. This behavior is expected because the gains of $K_P = -5 \times 10^{-4}$ and $K_D = 1.8$

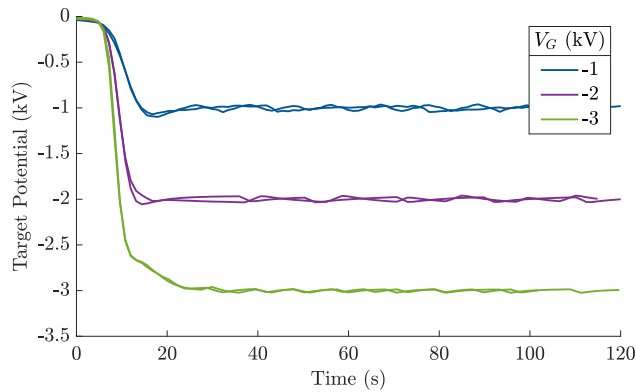


Fig. 6. Six trials of CACC as measured by the Trek probe for a 10-keV electron beam.

were tuned specially for a $\phi_G = -2$ kV. However, even with the suboptimal gains, each of the trials converges to the goal potential. Also, at the steady state, for $\phi_G = -2$ kV and $\phi_G = -3$ kV, the oscillations are 40 and 24 V, respectively. This corresponds to a 2% error and 0.8% error, respectively. Even for $\phi_G = -1$ kV, where the oscillations are up to 46 V, this is only a 4.6% error in the final potential. Using both proportional and derivative control, a goal potential can be achieved on a target in tens of seconds with less than 5% error.

At the beginning of each trial in Fig. 6, the target potential stays around zero for the first ≈ 5 s, even after the control is applied. For the beam energies used here, measurable current is not emitted from the electron beam until the grid voltage is below 50 V (the exact value varies with beam energy). For each trial, the initial grid potential was 60 V to ensure no significant charging occurs until after control is applied. After the grid potential decreased below 50 V at ≈ 5 s, charging occurred quickly.

These experiments demonstrate that, in a vacuum chamber environment, CACC can be used for actively controlling the electric potential of a floating target object. They also demonstrate the importance of selecting the correct gains, as untuned gains lead to long convergence times and even instabilities. More results demonstrating CACC in a vacuum chamber environment are presented in [56]. The viability of CACC in a more realistic environment is addressed in the following section.

C. Energy-Based ACC

An alternate approach considered is to vary the e-beam energy to control the target potential. The controller described by (12) is implemented here. However, during these experiments, very small derivative gains were used (on the order of -1×10^{-4}). The resulting control due to the derivative control was orders of magnitude smaller than that of the proportional control. Additional experiments confirmed that increasing/decreasing the derivative gain, but maintaining a similar order of magnitude, did not affect the charging behavior. Because the effect of the derivative control was negligible, the following experiments and analysis assume a linear proportional controller for EACC ($K_D = 0$).

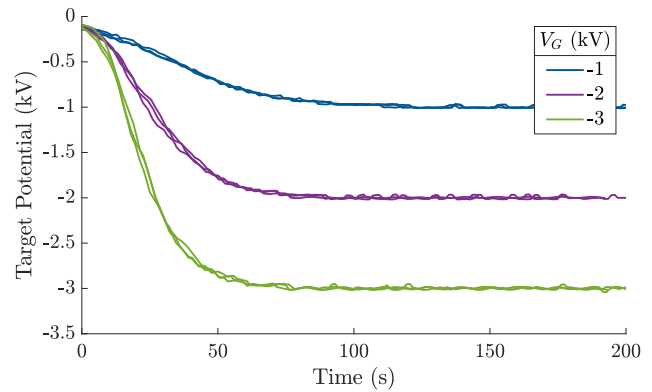


Fig. 7. Nine trials of EACC as measured by the Trek probe.

Fig. 7 shows nine trials of this control with a varying goal potential and a gain value of $K_P = 0.1$. For these trials, the impacting current was held at around $2 \mu\text{A}$ such that the resulting electron beam current and secondary/backscattered currents dominated the system. The emitted beam current decreased slightly as the cathode of the electron gun was used, but the overall current was kept large enough that a change in beam current did not affect the charging behavior of the target.

For the three trials with goal potential $\phi_G = -1$ kV, the maximum error is 35.5 V, or 3.6% of the goal potential. For goal potentials of $\phi_G = -2$ kV and $\phi_G = -3$ kV, the respective maximum errors are 37 V (1.9%) and 50 V (1.7%). The trials shown in Fig. 7 were not tuned for a specific scenario, but are included to show the consistency of EACC. For all three scenarios, all three independent trials exhibit nearly identical behavior. Each of these trials converged to steady-state behavior about the goal potential within 100 s; however, the convergence time can be decreased by tuning the gain of the trials.

For the experiments, in the LabVIEW program, the applied control was delayed by one time step: at time step $k = 1$, u_0 was applied. At time step $k = 2$, the control u_1 is applied and so on. In Fig. 7, because the gains are relatively small, the control applied at each time was very similar, so, while this is not the exact behavior expected from the controller, it is similar.

V. NUMERICAL ANALYSIS OF E-BEAM-BASED ACC

As described previously, both a VUV lamp and an electron beam are required to fully control a target's potential in a general space environment with CACC. A second instrument complicates the power requirements and design constraints of a potential mission. Accurately directing two instruments further complicates pointing constraints as well. Also, both these ACC methods are explored for an ideal vacuum chamber environment with a single target, but this will not be the case for in situ applications. Realistic charging scenarios include a variable space environment and coupled charging behavior between a servicer and target. Exploring the relationship between beam current/energy and target potential in a realistic environment provides insights into the feasibility of these two

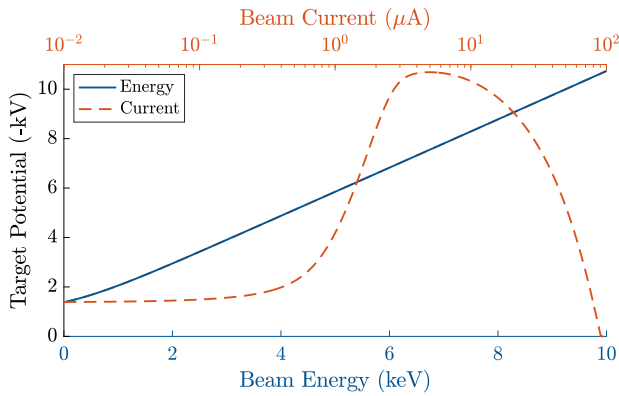


Fig. 8. Effects of e-beam current and energy on target potential in a calm geostationary environment.

controllers. A parametric study is performed to determine this relationship for a range of beam energies and currents in a calm geostationary environment.

To complete this study, beam energy and beam current were independently varied, and the steady-state potential of the target object was computed. When energy was varied between 0 keV and 10 keV, the beam current was held constant at 10 μA . When the current was varied between 10 nA and 10 mA, the beam energy was held constant at 10 keV. Each numeric trial was performed considering a calm geostationary environment for a satellite in eclipse. A similar study is conducted in [15]. Fig. 8 shows how the steady-state potential of the target evolves with the changing beam parameters. The two spacecraft are 1-m radius aluminum spheres.

Increasing the beam current does not exclusively decrease the target potential. Starting at a very small beam current, the electron beam does not significantly affect the target. As the current increases, the electron beam dominates over the environment, and the target charges become more negative than the natural floating potential. But once the beam current increases past a critical value, the target begins to charge more positively. This occurs because, as current is emitted, the servicer also charges positive. The difference in potentials between the target and the servicer cannot exceed the beam energy, so for the servicer's potential to continue increasing, the target potential must also increase [15]. The result is a nonmonotonic function that actually shows that, in a more realistic environment, manipulating only the beam current can both increase and decrease the potential of the target. However, the linear PD controller presented in Section II would not be feasible for CACC, as it is possible to end up in a region where increasing/decreasing the beam current does not drive the target to the desired equilibrium. Increasing the beam energy, on the other hand, results in a monotonic function with the target potential decreasing as the beam energy increases. This behavior continues across all increasing beam energies, testing up to 100 keV. This is a linear monotonic relationship (after exceeding 2.1 keV), which suggests that the controller outlined in Section II is sufficient for ACC in a realistic charging scenario. As such, a numeric model is built for simulating EACC, and the stability of the controller is evaluated.

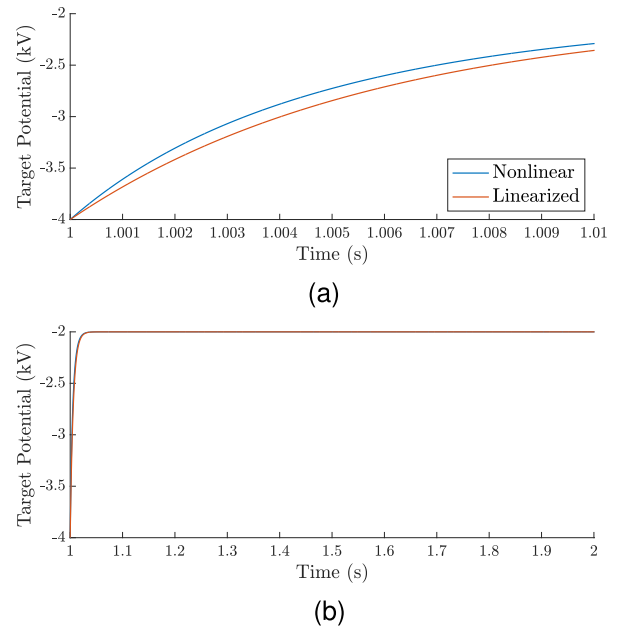


Fig. 9. Comparison between the nonlinear charging equation given by (13) and linearized charging equation of (14). (a) First 10 ms after control is applied. (b) First 1 s after control is applied.

A. Stability Analysis

To discuss the stability of the control, the nonlinear differential equation in (13) is linearized about the steady-state values, $E_{EB} = E_G$ and $\phi_T = \phi_G$, where E_G is the beam energy required to achieve this goal potential. Performing a Taylor series expansion about the equilibrium point and removing the higher-order terms gives

$$\delta\dot{\mathbf{x}} = \begin{bmatrix} \delta\dot{\phi}_T \\ \delta\dot{E}_{EB} \end{bmatrix} = \frac{I_{EB}}{C_{sc}} \begin{bmatrix} a_m & a_m \\ 0 & 0 \end{bmatrix} \begin{bmatrix} \delta\phi_T \\ \delta E_{EB} \end{bmatrix} + \begin{bmatrix} 0 \\ 1 \end{bmatrix} \delta u \quad (14)$$

with

$$a_m = \left(c \left(-\frac{e^{-\frac{E_2}{a}}}{a} + \frac{e^{-\frac{E_2}{b}}}{b} \right) + BCe^{-CE_2} \right). \quad (15)$$

Note that (14) is of the form $\delta\dot{\mathbf{x}} = [A_m]\delta\mathbf{x} + [B_m]\delta u$. At equilibrium $\delta\phi_T = 0$ and $\delta\phi_{EB} = 0$. Additionally, it can be seen in (14) that ϕ_G and E_G do not appear. At a steady state, $\phi_T + E_{EB} = E_2$, so $\phi_G + E_G = E_2$ which allows for (14) to be further simplified. The comparison between the nonlinear and linearized equations presented by Fig. 9 shows that there is a good alignment between the two equations for small deviations about the equilibrium.

For an initial deviation of $\delta\mathbf{x} = [-2 \text{ kV}, 2 \text{ keV}]^T$ from the equilibrium point $\delta\mathbf{x}_{eq} = [-2 \text{ kV}, 6.46 \text{ keV}]^T$, it can be seen that the nonlinear and linearized behaviors are very similar. Over the first 0.01 s, there is a slight difference between the two functions, but over the course of the full time step, the two lines are nearly identical. Because the linearized charging equations accurately represent the nonlinear equations for small deviations about the equilibrium, the stability analysis is performed on the linearized equations.

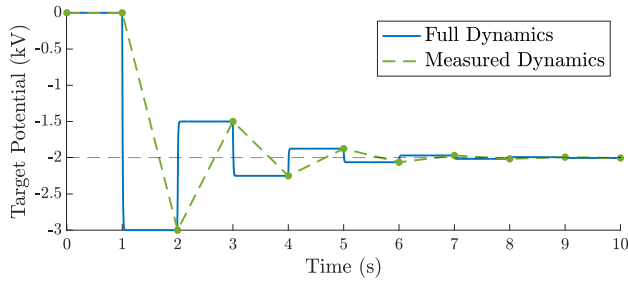


Fig. 10. Full simulated charging and “measured” potential of a target for EACC.

The control is applied directly after a measurement is taken; therefore, the frequency of control depends directly on the frequency of measurements. For the experiments presented earlier, a measurement was taken every 1.2 s. Here, control is applied every 1 s, but, as shown by Fig. 9, the charging dynamics occur over the span of 0.01 s. The target charges to its steady potential faster than it is measured and remains there until control is applied. Fig. 10 illustrates this by comparing the charging behavior measured by the servicer and the full charging dynamics of the target. Each point corresponds to a simulated measurement taken by the servicer. It can be seen that by the time the target’s potential is measured, the system has reached the steady state. Additionally, over each 1 s time step, the applied control is constant. This suggests that the control being applied here acts closer to a discrete control than a continuous control, and as such, (14) must be discretized.

To discretize the system, (14) must be converted into the linearized form $\delta\mathbf{x}_{k+1} = [F]\delta\mathbf{x}_k + [G]\delta u_k$, where k is the time step. The applied control is constant over each 1 s. This means that the control is a zero-order hold (ZOH) input over $\Delta t = 1$ s. Using this, an augmented state matrix can be built

$$\delta\dot{\mathbf{x}} = \begin{bmatrix} \frac{I_{EB}}{C_{sc}} a_m & \frac{I_{EB}}{C_{sc}} a_m & 0 \\ 0 & 0 & 1 \end{bmatrix} \begin{bmatrix} \delta\phi_T \\ \delta E_{EB} \\ \delta u \end{bmatrix} = [\hat{A}_m] \delta\dot{\mathbf{x}}. \quad (16)$$

Solving the above equation, the result is a matrix exponential of $[\hat{A}_m]\Delta t$, and the components of this matrix exponential give the $[F]$ and $[G]$ matrices of the discretized system

$$e^{\hat{A}_m \Delta t} = \begin{bmatrix} [F] & [G] \\ 0 & 1 \end{bmatrix}. \quad (17)$$

The final linearized discrete system for EACC is given by

$$\delta\mathbf{x}_{k+1} = \begin{bmatrix} e^\beta & e^\beta - 1 \\ 0 & 1 \end{bmatrix} \delta\mathbf{x}_k + \begin{bmatrix} -\frac{\beta - e^\beta + 1}{\beta} \\ 1 \end{bmatrix} \delta u_k \quad (18)$$

with

$$\beta = \frac{I_{EB}}{C_{sc}} \left(c \left(-\frac{1}{a} e^{-\frac{E_2}{a}} + \frac{1}{b} e^{-\frac{E_2}{b}} \right) + B C e^{-CE_2} \right). \quad (19)$$

One final simplification must be performed: computing δu_k by taking the gradient of u , with respect to \mathbf{x} . As described previously, derivative control is not required for quick convergence using EACC; therefore, the derivative control is ignored, and a proportional controller is used to apply control:

$u = K_P(\phi_{T_i} - \phi_G)$. This gives $\delta u_k = [K]\delta\mathbf{x}_k$, and 18 can be simplified to

$$\begin{aligned} \delta\mathbf{x}_{k+1} &= [F] \delta\mathbf{x}_k + [G] \delta u_k \\ &= [F] \delta\mathbf{x}_k + [G][K] \delta\mathbf{x}_k = ([F] + [G][K]) \delta\mathbf{x}_k \end{aligned} \quad (20)$$

with

$$[K] = [K_P, 0]. \quad (21)$$

Now that the discretized linear differential charging equation accurately describes the controller that has been determined, the stability of the control can be determined by examining the eigenvalues of $[F] + [G][K]$. For this discrete system to be stable, its absolute value must be less than one. This gives

$$|\lambda| = \left| \frac{\beta - K_P - K_P\beta \pm \sqrt{4K_P\beta + (K_P - \beta + K_P\beta)^2}}{2\beta} \right| < 1. \quad (22)$$

The value of β is dependent on material properties, but is dominated by target and beam properties. Initially, neglecting the I_{EB}/C_{sc} term, $\beta_{Au} = -0.144I_{EB}/C_{sc}$ for gold. For other common materials, like aluminum and gold paint (as used on SCATHA), $\beta_{Al} = -0.587I_{EB}/C_{sc}$ and $\beta_{paint} = -0.150I_{EB}/C_{sc}$. These values are computed using [1, Ch. 3, Table 3.1]. The SEY and BEY terms of β give a coefficient $-1 < \alpha < 0$ for $\beta = \alpha I_{EB}/C_{sc}$ using most common materials. On the other hand, realistic capacitance and beam current values are on the order of 0.1 nF and 0.1 mA. This gives $I_{EB}/C_{sc} \approx 10^6$, significantly larger than the material property contribution. As such, β does not significantly change between materials.

For the simulations presented in this article, $\beta = -173342$. This allows (22) to be solved and the resulting stability condition to be found

$$0 \leq K_P \leq 2.0001. \quad (23)$$

With the nonlinear system approximated as a linearized discrete system, this control is stable for small deviations about the equilibrium point as long as the control time is significantly larger than the charging time.

B. Numeric Model Validation

To validate the charging model described in Section II, experimental data from Section IV is compared to the numeric charging model. This means that the numeric model must be adapted to accurately reflect the physical system, including the time-shifted control, the 20 V measurement error, and realistic simulation parameters. Referring to (13), the values still explicitly needed are the capacitance of the target, C_{sc} , and impacting beam current, I_{EB} . Taking the average current measurement from the Faraday cup and extrapolating that to the entire disk, I_{EB} was estimated to be 2.0 μ A. The capacitance was computed for a thin disk and found to be 0.56 pF.

Additionally, the nonideal relationship between beam energy and target potential has to be accounted for. Fig. 5 shows that, for these experiments, the relationship between beam energy and target potential is linear with a slope of

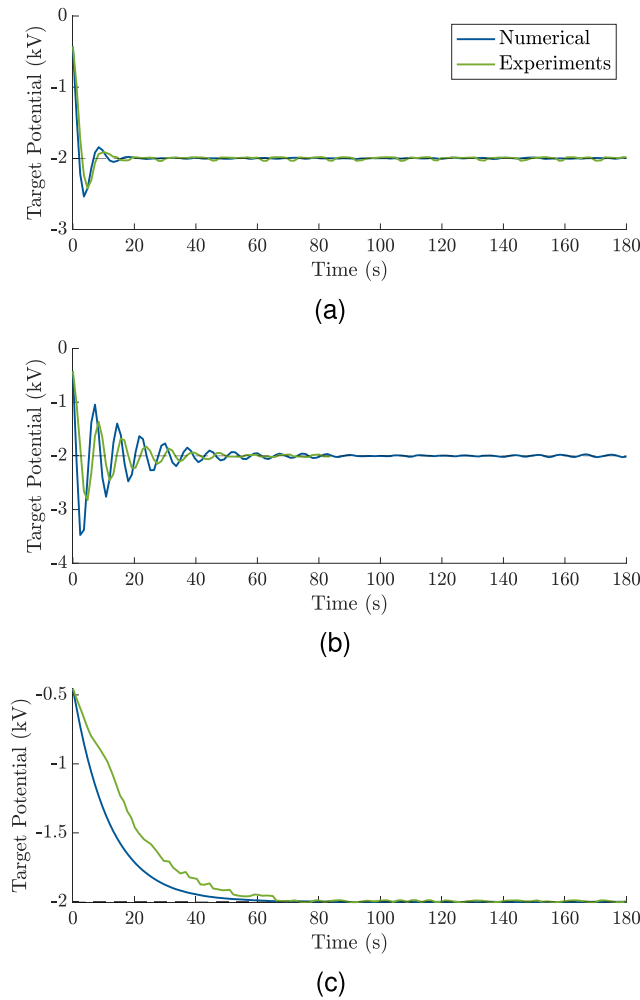


Fig. 11. Comparison between experimental and numerical results using EACC. (a) Slightly underdamped scenario. (b) Underdamped scenario. (c) Overdamped scenario.

-0.87 , contrary to the ideal model that predicts a slope of -1 . This discrepancy affects the steady-state charging. Increasing the beam energy by 100 eV in the experiments had the same effect as increasing the beam energy by 87 eV in the numerical simulations. This was accounted for by scaling the applied control by the actual slope m . Finally, to accurately compare the target's charging behavior, the difference in E_2 has to be accounted for. For the Sanders SEY model for gold, $E_{2,num} = 4.46$ keV while experimentally, $E_{2,exp} \approx 6.32$ keV. To account for this difference, the initial beam energy for the simulations is $E_{EB_0} = E_{2,num} + 400$ V and only experimental data after $\phi_T < -400$ V is considered. This ensures that the charging behavior is in the linear region of Fig. 5. Both these adjustments would be eliminated by a more accurate TEY.

A comparison of the charging model and experiments is shown in Fig. 11 for three charging scenarios. A time step of $10 \mu\text{s}$ is used in the numerical simulations. Each scenario has an initial potential of -0.4 kV and a goal potential of -2 kV. The gains are $K_p = 0.6$, $K_p = 1$, and $K_p = 0.1$ to represent a slightly underdamped, overdamped, and underdamped scenario, respectively. In each case, the numerical simulations show the same overall behavior as the experiments. The

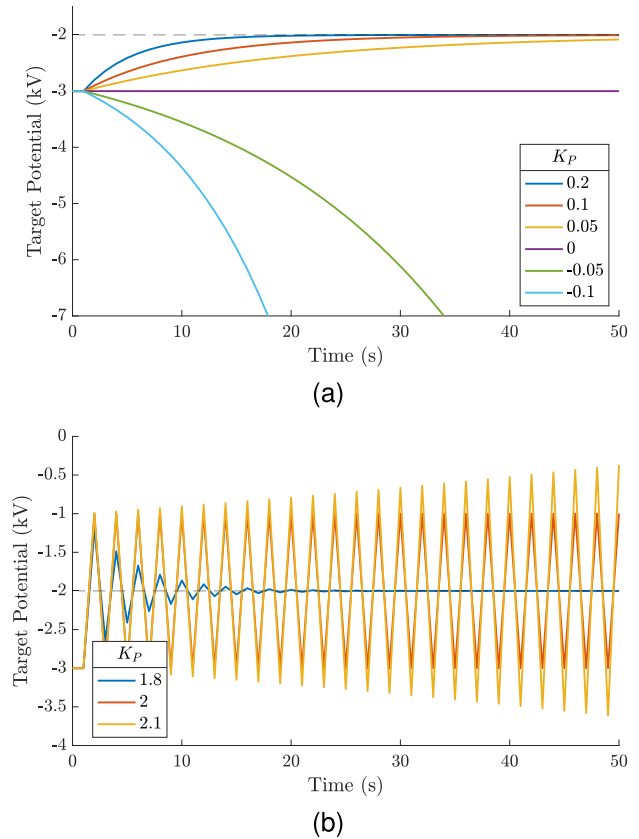


Fig. 12. Numerical analysis of EACC for gains around the stability condition of (23). (a) Gains around $K_p = 0$. (b) Gains around $K_p = 2$.

slightly underdamped trial is the most similar, with both lines being nearly on top of each other, while the other two deviate slightly more but are still very similar. These inconsistencies are likely due to the inaccurate TEY model. When the target potential is > -1 kV, the system is in the nonlinear region of Fig. 5(b) which is not accurately replicated using the numeric TEY. While all three scenarios are affected by this, the effect is most pronounced in Fig. 11(c) where the difference between experiments and simulations is greatest. Because the gain is small and the initial potential is -455 V, this system stays within the nonlinear region longest, and the differences build up. Once the target potential reaches -1 kV, the two curves display more similar behavior. Even with the inaccurate TEY model, the experimental results match the numeric results well, validating the EACC model for a vacuum chamber environment.

Now that the numeric model has been validated through matching the experimental results, more realistic charging scenarios are explored. Specifically, a gain analysis is performed to confirm the stability conditions determined in Section II. For a more realistic scenario, the target spacecraft is taken to be a conducting sphere with a radius of 1 m and the impacting beam current is $120 \mu\text{A}$. External currents are not simulated; therefore, these trials are representative of either a vacuum chamber environment or a space environment where the electron beam is the dominating current.

Fig. 12 presents multiple trials for gains around the stability limits $K_p = 0$ and $K_p = 2$. For these trials, the initial state is

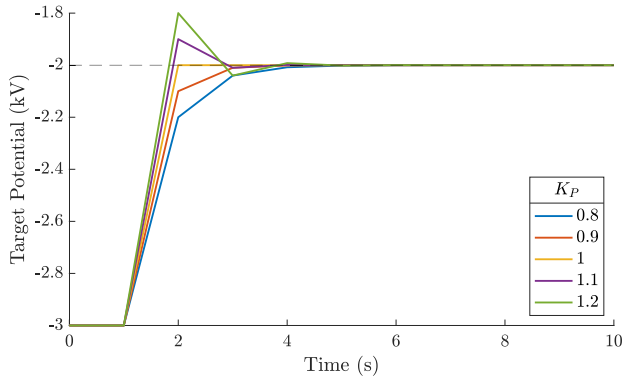


Fig. 13. Investigation into the charging behavior for gains around $K_p = 1$.

$\phi_T = -3$ kV and $E_{EB} = 7.46$ keV. The goal potential is -2 kV. According to the charging equations, the target will not charge for the first time step, after which control is applied. These results are consistent with the condition in (23) that the proportional gain must be between 0 and 2. The results for the negative gain in Fig. 12 make sense because it has been shown that E_{EB} and ϕ_T have a monotonically decreasing relationship. With a negative gain, a negative error will increase the beam energy, which drives the target potential more negative, further increasing the magnitude of the error. Gains less than 2 yield underdamped systems, while a gain of exactly 2 is marginally stable about the desired potential. For gains greater than 2, the system is unstable, with the magnitude of the error continually increasing with time.

With the stability condition supported by numerical simulations, a gain analysis about $K_p = 1$ is performed under the same conditions. Fig. 13 shows the results. Each of the trials converges within 5 s, meaning it takes a maximum of four measurements to reach the goal potential. Any gain less than 1 results in an overdamped system, while any gain greater than 1 is an underdamped system. For a gain of 1, the goal potential is achieved after the first control instance. For an ideal scenario, this is expected. With $K_p = 1$, the control is equal to the error, $\delta E_{EB} = \delta \phi_T$, and increasing E_{EB} decreases ϕ_T the same amount. In other words, increasing the beam energy by $\phi_T - \phi_G$ will decrease the target potential by $\phi_T - \phi_G$ such that the new potential is $\phi_{T_{k+1}} = \phi_{T_k} - (\phi_{T_k} - \phi_G) = \phi_G$.

C. Uncertainty Analysis

1) *SEY Parameters:* While it is useful for analysis, ideal scenarios rarely occur. Charging spacecraft are subject to significant uncertainty. The TEY depends significantly on material and surface properties, which can change significantly over the course of a mission through mechanisms like out-gassing, UV light exposure, and micrometeorite/space debris impacts [57], [58]. Spacecraft have complex shapes/compositions, which affect the capacitance of the system, and output beam properties may not be exactly the same as the input parameters. All these factors are important to the ACC model. To investigate how uncertainty in SEY affects EACC, 400 Monte Carlo trials with 20 uniform sampling each of $E_{max} \sim \mathcal{U}(0.6, 1)$ keV and $\delta_{max} \sim \mathcal{U}(1.09, 1.81)$ are conducted. These ranges correspond to the nominal values for gold $\pm 25\%$. Fig. 14

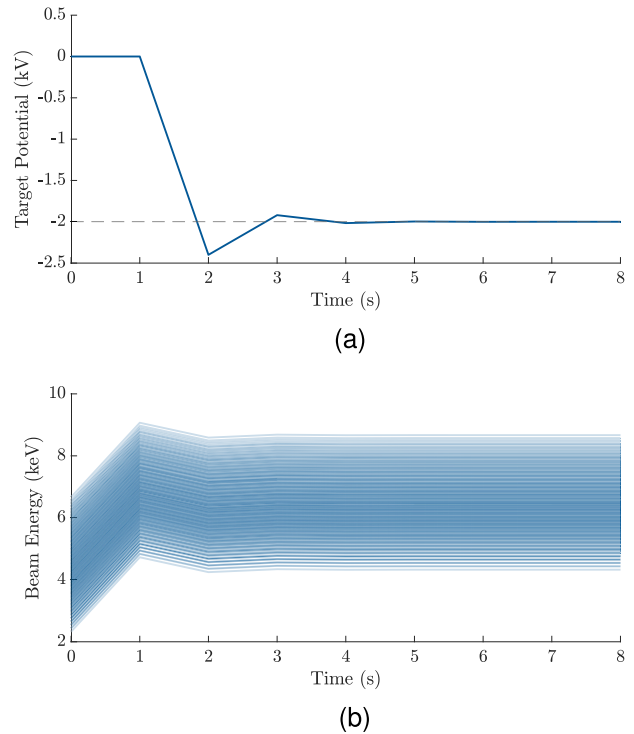


Fig. 14. Charging behavior of 400 Monte Carlo trials varying the SEY parameters of δ_{max} and E_{max} . (a) Target potential versus time. (b) Beam energy versus time.

shows the charging behavior and beam energies of each of the 400 trials.

The target charging behavior is exactly the same for each trial. Regardless of the actual SEY parameters, in these ideal simulations, beam energy and target potential have a linear one-to-one relationship for $E \geq E_2$ regardless of the actual E_2 value. Also, each trial is started with an initial state of $\mathbf{x}_0 = [\phi_{T_0}, E_{EB_0}]^T = [0, E_2]^T$. The target will remain ≈ 0 V until the beam energy exceeds E_2 , so this initial state corresponds to the first time instance where the nonzero charging occurs. Each trial is started in the region where $E \geq E_2$, so regardless of material properties, increasing the beam energy will decrease the target potential by the same amount. The only change is that E_2 is different for each set of parameters, so the beam energy required to induce each potential on the target is different. These results suggest that as long as the electron beam has a sufficiently high maximum energy, the charging behavior of the target will be the same regardless of uncertainty in material properties. Uncertainty in the BEY parameters has the same behavior as that demonstrated for SEY parameters.

When the material has $\delta_{max} < 1$ at a normal incidence angle, this control is not applicable: the TEY is never equal to one, and the target will charge to $\phi_T \approx -E_{EB}$. When this occurs, there is no way to discharge the target if the control overshoots the goal potential. If after one time step, the beam energy is 2.5 keV, the target charges to -2.5 kV. For a goal potential of -2 kV and $K_p = 1$, the control decreases the beam energy to 2 keV; however, now the beam energy is less than the target potential and no longer impacts the target. There are a few conducting materials, such as pure aluminum, that

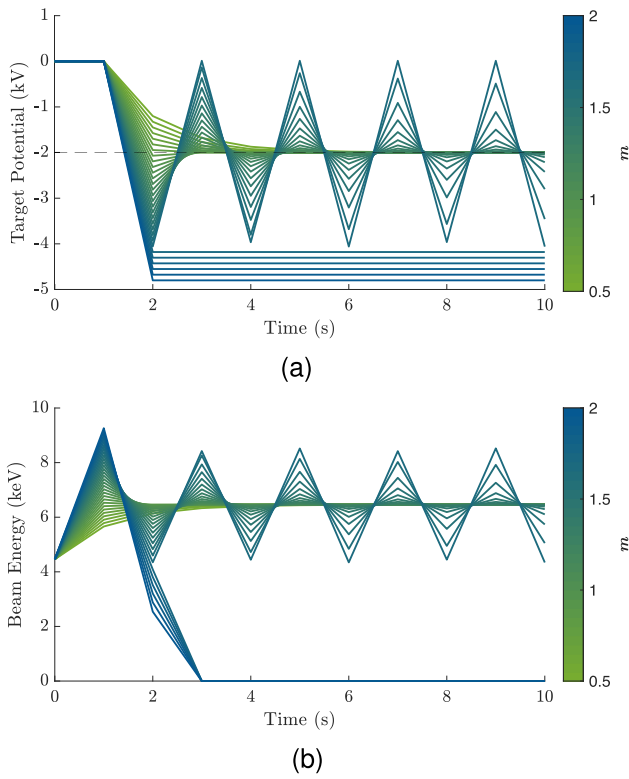


Fig. 15. Charging behavior of 30 Monte Carlo trials varying the slope of the linear relationship between ϕ_T and E_{EB} . (a) Target potential versus time. (b) Beam energy versus time.

have $\delta_{\max} < 1$ ($\delta_{\max_{AI}} = 0.97$); however, any exposure to air leads to the rapid formation of oxides and contamination layers that typically increase the yield [40], [49]. If the TEY never exceeds one for the specific material, a different control must be implemented.

Fig. 14 shows how uncertainty in the parameters in SEY affects the charge control behavior, but there is also uncertainty in the relationship between beam energy and target potential. Fig. 5 shows that even in highly controlled experiments, E_{EB} and ϕ_T have a linear relationship but with a slope, m , of -0.87 not -1 . Fig. 15 shows how variations in this relationship affect EACC. The slope m is sampled $200\times$ with $m \sim \mathcal{U}(0.5, 2)$; however, only 30 are shown in Fig. 15. Technically, m is the absolute value of the slope between E_{EB} and ϕ_T as the negative relationship is inherently accounted for. The other parameters for these trials are, $\mathbf{x}_0 = [0, E_2]^T$, $\phi_G = -2$ kV, and $K_P = 1.2$. It can be seen that the data presented in Fig. 15 resembles that of the gain searches shown in Figs. 12 and 13.

With variation in these m parameters, some of the trials in Fig. 15 become unstable. This can be seen in one trial that has a slowly increasing oscillation amplitude and the multiple trials where the target potential becomes a constant other than ϕ_G and the beam energy goes to 0 eV. This occurs because, at 2 s for these trials, the control decreases the beam energy such that $-\phi_T > E_{EB}$. Referencing (2), at this point, the electrons no longer impact the target and the net current becomes 0 A. Removing this constraint, the control is still unstable. Based on these results, uncertainty in the actual SEY model can have a significant effect on the charging behavior and result

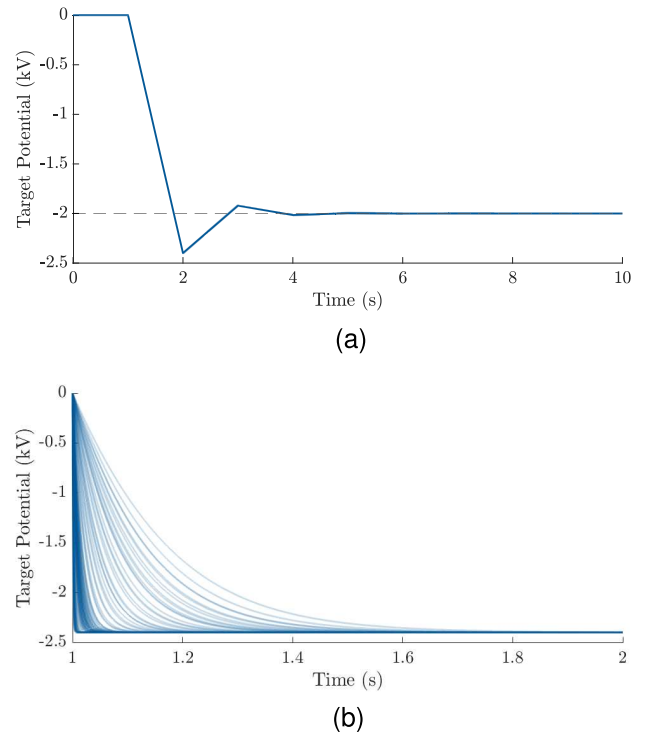


Fig. 16. Charging behavior of 100 Monte Carlo trials with varying capacitances and beam currents. (a) Full 10 s. (b) First 1 s after control is applied.

in unstable control. A quality estimate for m is necessary to have confidence in the controller. However, taking a closer look at the controller, this is not as significant a concern as it appears. The value m scales how much the change in beam energy affects the target potential. Given that this is a linear relationship, this can be flipped, such that a $1/m$ scales how the change in target potential affects the change in beam energy. Applying (12) (disregarding the derivative control, that is, $K_D = 0$) to (13), $\dot{E}_{EB} = K_P(\phi_T - \phi_G)$. Here, $(\phi_T - \phi_G)$ is the change in target potential, so m can be included as $\dot{E}_{EB} = K_P/m(\phi_T - \phi_G)$. Because m is a constant for each trial, it can be absorbed into the gain; however, this alters the stability condition of (23). Now, $0 \leq mK_P \leq 2$. Because E_{EB} and ϕ_T will never have a positive relationship, if it can be guaranteed that $0 < m \leq 1$, uncertainty in m will only cause inefficiencies in the controller, never instabilities.

2) *Spacecraft and Equipment Parameters*: For in situ applications, given the numerous components and different materials, the capacitance of the spacecraft will not be exactly known. Additionally, the exact current emitted from the electron beam will also not be constant; as the electron gun operates, the cathode inside degrades, leading to fewer electrons being emitted. These two parameters appear directly in (13) and as such will affect the charging behavior. To explore this, 100 Monte Carlo trials with C_{sc} and I_{EB} varying between [50 pF, 1 nF] and [50, 500] μ A, respectively, are shown by Fig. 16. These capacitances correspond to spheres with radii between 0.45 and 9 m.

In Fig. 16(a), for all trials, the charging behavior, as seen by the servicer with 1 s measurements, is identical. This suggests that any change caused by varying the target capacitance and impacting beam current occurs within one second.

Fig. 16(b) shows the actual charging behavior over the first second that control is applied. The main difference between each trial is how quickly they reach the steady-state potential of -2.4 kV. In 13, C_{sc} and I_{EB} only affect the magnitude of $\dot{\phi}_T$: any uncertainty in these values would only change the convergence time, not the actual steady state value. Each trial converges within 1 s, before the servicer measures the target potential, and therefore does not affect the control. If the sample time is shorter, or the value of I_{EB}/C_{sc} becomes very small, then the target will not converge to its steady state behavior before a measurement is taken. When this occurs, the system can no longer be approximated as a discrete system. The stability conditions would need to be re-derived for the linearized continuous system described in (14). However, these conditions are not realistic for typical satellites as they require either a spacecraft with $C_{sc} > 3$ nF (a sphere with a radius > 27 m) or $I_{EB} < 4.5$ μ A.

VI. CONCLUSION

The objective of this article is to develop a technique for actively controlling the electrostatic potential of an uncontrolled vacuum chamber target using an electron beam. Two methods are presented, applying control to different beam parameters: electron beam current and electron beam energy. Both methods are performed in an ideal vacuum chamber environment. Electron beam energy control is determined to be more applicable due to fewer instrument requirements and a monotonically decreasing relationship between target potential and beam energy in a realistic environment; however, both are valid methods in a vacuum chamber environment.

For EACC, a numeric charging model is developed and compared to the vacuum chamber experiments. The same charging behavior is seen in both the experiments and the numerical simulations, validating the numerical model. The linear proportional controller used for control is proved to be stable for small deviations about an equilibrium point, given the proportional gain has a value between zero and two. A gain analysis using these numerical models confirms the stability condition applied to the proportional gain and shows that, for an ideal system, with a proportional gain equal to one, the control will converge after a single measurement.

Uncertainty is investigated through Monte Carlo trials, varying the TEY parameters, target capacitance, and impacting beam current. For realistic variations in the secondary electron parameters, target capacitance, and beam current, the charging behavior of the target, as measured by the servicer, is unchanged, but the required beam energy can be affected. As long as the maximum beam energy is large enough, uncertainty in these parameters will not affect the control. Uncertainty in the actual SEY model, however, will affect the stability conditions of the control. When the slope of the relationship between beam energy and target potential is not -1 , previously stable gains may no longer be stable. Assuming the relationship is still linear, the stability constraint gets scaled by the slope, which may cause inefficiencies and, if large enough, instabilities in the control. However, this relationship can be estimated in situ before applying control by measuring the target potential achieved by a variety of beam energies

and then estimating the slope of the linear section of this relationship, reducing this uncertainty.

ACKNOWLEDGMENT

The authors would like to thank the members of the Spacecraft Charging and Instrument Calibration Laboratory at the Air Force Research Laboratory for their support and use of their facilities.

REFERENCES

- [1] S. T. Lai, *Fundamentals of Spacecraft Charging*. Princeton, NJ, USA: Princeton Univ. Press, Oct. 2011.
- [2] C. R. Seubert, L. A. Stiles, and H. Schaub, "Effective Coulomb force modeling for spacecraft in Earth orbit plasmas," *Adv. Space Res.*, vol. 54, no. 2, pp. 209–220, Jul. 2014.
- [3] M. H. Denton, M. F. Thomsen, H. Korth, S. Lynch, J. C. Zhang, and M. W. Liemohn, "Bulk plasma properties at geosynchronous orbit," *J. Geophys. Res., Space Phys.*, vol. 110, no. A7, Jul. 2005.
- [4] NASA.(2022). *2022 Nasa Strategic Plan*. Accessed: May 15, 2025. [Online]. Available: <https://www.nasa.gov/ocfo/strategic-plan/>
- [5] M. Smith et al., "The Artemis program: An overview of NASA's activities to return humans to the moon," in *Proc. IEEE Aerosp. Conf.*, Mar. 2020, pp. 1–10.
- [6] S. Sakai et al., "Moon landing results of SLIM: A smart lander for investigating the moon," *Acta Astronautica*, vol. 235, pp. 47–54, Oct. 2025.
- [7] C. Wang et al., "Scientific objectives and payload configuration of the Chang'E-7 mission," *Nat. Sci. Rev.*, vol. 11, no. 2, Jan. 2024.
- [8] F. B. Leahy. (2021). *SLS-SPEC-159, Cross-Program Design Specification for Natural Environments (DSNE)*. [Online]. Available: <https://ntrs.nasa.gov/citations/20210024522>
- [9] K. Champion and H. Schaub, "Electrostatic potential shielding in representative cislunar regions," *IEEE Trans. Plasma Sci.*, vol. 51, no. 9, pp. 2482–2500, Sep. 2023.
- [10] C. R. Francis, "Electrostatic charging problems of spacecraft," *J. Electrostatics*, vol. 11, no. 3, pp. 265–280, Feb. 1982.
- [11] H. C. Koons and D. J. Gorney, "Relationship between electrostatic discharges on spacecraft P78–2 and the electron environment," *J. Spacecraft Rockets*, vol. 28, no. 6, pp. 683–688, Nov. 1991.
- [12] C. K. Purvis, H. B. Garrett, A. C. Whittlesey, and N. J. Stevens. (1984). *Design Guidelines for Assessing and Controlling Spacecraft Charging Effects. National Aeronautics and Space Administration*. [Online]. Available: <https://ntrs.nasa.gov/citations/19840025381>
- [13] R. Gubby and J. Evans, "Space environment effects and satellite design," *J. Atmos. Solar-Terrestrial Phys.*, vol. 64, no. 16, pp. 1723–1733, Nov. 2002.
- [14] R. C. Olsen, "The hidden ion population of the magnetosphere," *J. Geophys. Research: Space Phys.*, vol. 87, no. A5, pp. 3481–3488, May 1982.
- [15] H. Schaub and Z. Sternovsky, "Active space debris charging for contactless electrostatic disposal maneuvers," *Adv. Space Res.*, vol. 53, no. 1, pp. 110–118, Jan. 2014.
- [16] L. B. King, G. G. Parker, S. Deshmukh, and J.-H. Chong, "Study of interspacecraft Coulomb forces and implications for formation flying," *J. Propuls. Power*, vol. 19, no. 3, pp. 497–505, May 2003.
- [17] H. Schaub, G. G. Parker, and L. B. King, "Challenges and prospects of Coulomb spacecraft formations," *Adv. Astron. Sci.*, vol. 115, no. June, pp. 351–370, 2003.
- [18] K. Wilson and H. Schaub, "Impact of electrostatic perturbations on proximity operations in high Earth orbits," *J. Spacecraft Rockets*, vol. 58, no. 5, pp. 1–10, Sep. 2021.
- [19] K. Wilson and H. Schaub, "Constrained guidance for spacecraft proximity operations under electrostatic perturbations," in *Proc. IEEE Aerosp. Eng. Conf.*, Mar. 2022, pp. 1–11.
- [20] K. Wilson, A. Romero-Calvo, and H. Schaub, "Constrained guidance for spacecraft proximity operations under electrostatic perturbations," *J. Spacecraft Rockets*, vol. 59, no. 4, pp. 1304–1316, Jul. 2022.
- [21] H. Schaub, G. G. Parker, and L. B. King, "Challenges and prospect of Coulomb formations," *J. Astron. Sci.*, vol. 52, nos. 1–2, pp. 169–193, Jun. 2004.
- [22] T. Bennett and H. Schaub, "Contactless electrostatic detumbling of axisymmetric GEO objects with nominal pushing or pulling," *Adv. Space Res.*, vol. 62, no. 11, pp. 2977–2987, Dec. 2018.

- [23] F. Casale, H. Schaub, and J. Douglas Biggs, "Lyapunov optimal touchless electrostatic detumbling of space debris in GEO using a surface multisphere model," *J. Spacecraft Rockets*, vol. 58, no. 3, pp. 764–778, May 2021.
- [24] H. Schaub and D. Stevenson, "Prospects of relative attitude control using Coulomb actuation," *J. Astron. Sci.*, vol. 60, nos. 3–4, pp. 258–277, Dec. 2013.
- [25] H. Schaub and D. F. Moorer, "Geosynchronous large debris reorbiter: Challenges and prospects," *J. Astron. Sci.*, vol. 59, nos. 1–2, pp. 161–176, Jun. 2012.
- [26] H. Schaub and L. E. Z. Jasper, "Circular orbit radius control using electrostatic actuation for 2-craft configurations," in *Proc. AAS/AIAA Astrodynamics Specialist Conf.*, Aug. 2011.
- [27] R. C. Olsen, "Experiments in charge control at geosynchronous orbit-ATS-5 and ATS-6," *J. Spacecraft Rockets*, vol. 22, no. 3, pp. 254–264, May 1985.
- [28] P. R. Stannard et al. (1980). *Analysis of the Charging of the Scatha (P78-2) Satellite*. [Online]. Available: <https://ntrs.nasa.gov/citations/19810018631>
- [29] C. K. Purvis, R. O. Bartlett, and S. E. Deforest, "Active control of spacecraft charging on ATS-5 and ATS-6," in *Proc. Spacecraft Charging Technol. Conf.*, Feb. 1977, pp. 107–120. [Online]. Available: <https://ntrs.nasa.gov/citations/19780002193>
- [30] W. Riedler et al., "Active spacecraft potential control," *Space Sci. Rev.*, vol. 79, pp. 271–302, Feb. 1997.
- [31] K. Torkar et al., "Active spacecraft potential control for cluster-implementation and first results," *Ann. Geophys.*, vol. 19, no. 10/12, pp. 1289–1302, 2001.
- [32] K. Torkar et al., "Spacecraft potential control aboard equator-S as a test for cluster-II," *Annales Geophysicae*, vol. 17, no. 12, p. 1582, 1999.
- [33] K. Torkar et al., "Spacecraft potential control for double star," *Annales Geophysicae*, vol. 23, no. 8, pp. 2813–2823, Nov. 2005.
- [34] K. Torkar et al., "Active spacecraft potential control investigation," *Space Sci. Rev.*, vol. 199, nos. 1–4, pp. 515–544, Mar. 2016.
- [35] R. Schmidt et al., "Results from active spacecraft potential control on the geotail spacecraft," *J. Geophys. Res., Space Phys.*, vol. 100, no. A9, pp. 17253–17259, Sep. 1995.
- [36] C. R. Seubert and H. Schaub, "Closed-loop charged relative motion experiments simulating constrained orbital motion," *J. Guid., Control, Dyn.*, vol. 33, no. 6, pp. 1856–1865, Nov. 2010.
- [37] T. Bennett, D. Stevenson, E. Hogan, L. McManus, and H. Schaub, "Prospects and challenges of touchless debris despinning using electrostatics," *Adv. Space Res.*, vol. 56, no. 3, pp. 557–568, Aug. 2015.
- [38] M. Bengtson, K. T. H. Wilson, and H. Schaub, "Simulations and experimental results of electron method for remote spacecraft charge sensing," in *Proc. Appl. Space Environ. Conf.*, May 2019.
- [39] K. Wilson and H. Schaub, "X-ray spectroscopy for electrostatic potential and material determination of space objects," *IEEE Trans. Plasma Sci.*, vol. 47, no. 8, pp. 3858–3866, Aug. 2019.
- [40] P. Lundgreen and J. R. Dennison, "Strategies for determining electron yield material parameters for spacecraft charge modeling," *Space Weather*, vol. 18, no. 4, Apr. 2020.
- [41] B. T. Draine and E. E. Salpeter, "On the physics of dust grains in hot gas," *Astrophys. J.*, vol. 231, pp. 77–94, Jul. 1979.
- [42] M. J. Mandell, J. M. Harvey, and I. Katz. (1997). *Nascap User Manual*. National Aeronautics and Space Administration. [Online]. Available: <https://ntrs.nasa.gov/citations/19780005386>
- [43] B. Thiébault, J. C. M. Velez, J. Forest, P. Sarraïll, and B. Jeanty-Ruard. (2019). *SPIS 6 User Manual*. [Online]. Available: <https://www.spis.org/software/spis/documentation/>
- [44] N. L. Sanders and G. T. Inouye, "Secondary emission effects on spacecraft charging: Energy distribution considerations," in *Proc. Spacecraft Charging Technol.*, 1978, pp. 747–755.
- [45] S. M. L. Prokopenko and J. G. Laframboise, "High-voltage differential charging of geostationary spacecraft," *J. Geophys. Res., Space Phys.*, vol. 85, no. A8, pp. 4125–4131, Aug. 1980.
- [46] R. C. Hoffmann, "Electron-induced electron yields of uncharged insulating materials," M.S. thesis, Dept. Phys., Utah State Univ., Logan, UT, USA, 2010.
- [47] J. Hammerl and H. Schaub, "Coupled spacecraft charging due to continuous electron beam emission and impact," *J. Spacecraft Rockets*, vol. 61, no. 5, pp. 1258–1271, Sep. 2024.
- [48] R. Cooper and R. Hoffman, "Jumbo space environment simulation and spacecraft charging chamber characterization," *Air Force Research Laboratory, Wright-Patterson Air Force Base, OH, USA, Tech. AFRL-RV-PS-TP-2015-0012*, 2015.
- [49] V. Baglin et al., "The secondary electron yield of technical materials and its variation with surface treatments," in *Proc. 7th Eur. Part. Accel. Conf.*, 2000.
- [50] W. M. Hayes, *CRC Handbook of Chemistry and Physics*, 95th ed., Boca Raton, FL, USA: CRC Press, 2014.
- [51] G. Wilson and J. R. Dennison, "Approximation of range in materials as a function of incident electron energy," *IEEE Trans. Plasma Sci.*, vol. 40, no. 2, pp. 291–297, Feb. 2012.
- [52] G. Wilson and J. Dennison, "Approximation of range in materials as a function of incident electron energy," in *Proc. 11th Spacecraft Charging Technol. Conf.*, vol. 40, 2010, pp. 291–297. [Online]. Available: <https://digitalcommons.usu.edu/physicsfacpub/1458>
- [53] I. Bojko, N. Hilleret, and C. Scheuerlein, "Influence of air exposures and thermal treatments on the secondary electron yield of copper," *J. Vac. Sci. Technol. A: Vac., Surf., Films*, vol. 18, no. 3, pp. 972–979, May 2000.
- [54] A. Bentabet, "Monte Carlo calculation of slow electron beam transport in solids: Reflection coefficient theory implications," *Modern Phys. Lett. B*, vol. 26, no. 4, Feb. 2012, Art. no. 1150022.
- [55] S. Valkealahti and R. M. Nieminen, "Monte-carlo calculations of keV electron and positron slowing down in solids," *Appl. Phys. A Solids Surf.*, vol. 32, no. 2, pp. 95–106, Oct. 1983.
- [56] J. D. Walker and H. Schaub, "Active charge control using an electron beam and ultraviolet light source," in *Proc. AIAA SCITECH Forum*, Jan. 2024.
- [57] E. R. Crutcher, L. S. Nishimura, K. Warner, and W. W. Wascher, "Migration and generation of contaminants from launch through recovery: LDEF case history," in *Proc. 1st 69 Months Space, Post-Retr. Symp.*, vol. 3134, 1991, pp. 121–140. [Online]. Available: <https://ntrs.nasa.gov/citations/19920014044>
- [58] A. C. Tribble, B. Boyadjian, J. Davis, J. Haffner, and E. McCullough. (1996). *Contamination Control Engineering Design Guidelines for the Aerospace Community*. [Online]. Available: <https://ntrs.nasa.gov/citations/19960044619>



James D. Walker III received the bachelor's degree in mechanical engineering from California Institute of Technology, Pasadena, CA, USA, in 2021, and the M.S. degree in aerospace engineering from the University of Colorado Boulder, Boulder, CO, USA, in 2024, where he is currently pursuing the Ph.D. degree with the Autonomous Vehicle Systems Laboratory, Aerospace Engineering Sciences Department.

His research interests include charged astrodynamics, spacecraft–plasma interactions, active space debris removal, and vacuum chamber experiments.

Mr. Walker received the Department of Defense National Defense Science and Engineering Graduate Fellowship in 2023.



Hanspeter Schaub is a Distinguished Professor and the Chair of the Aerospace Engineering Sciences Department, University of Colorado Boulder, Boulder, CO, USA. He holds the Schaden Leadership Chair. He has over 30 years of research experience, of which four years are at Sandia National Laboratories, Albuquerque, NM, USA. His research interests are in astrodynamics, relative motion dynamics, charged spacecraft motion, as well as spacecraft autonomy. This has led to about 228 journal and 371 conference publications, as well as a fourth edition textbook on *Analytical Mechanics of Space Systems*.

Dr. Schaub is a fellow of AIAA and AAS and a member of the National Academy of Engineering in 2025. In 2023, he won the Hazel Barnes Prize, the Top Award Granted to Faculty at the University of Colorado. He has been awarded the H. Joseph Smead Faculty Fellowship, the Provost's Faculty Achievement Award, the Faculty Assembly Award for Excellence in Teaching, and the Outstanding Faculty Advisor Award. He has won the AIAA/ASEE Atwood Educator Award, the AIAA Mechanics and Control of Flight Award, and the Collegiate Educator of the Year for the AIAA Rocky Mountain Section. He has been the ADCS Lead in the CICERO Mission, the ADCS Algorithm Lead in the Mars Mission, and supporting ADCS for a New Asteroid Mission.